UDC 681.7.066.63

Yu.S. Hordieiev, A.V. Zaichuk

TUNGSTEN-MODIFIED BARIUM-ALUMINUM-BORATE GLASSES WITH TUNABLE THERMAL BEHAVIOR AND ENHANCED GAMMA-RAY SHIELDING

Ukrainian State University of Science and Technologies, Dnipro, Ukraine

Radiation shielding glasses that avoid lead while retaining high attenuation efficiency remain a materials priority for medical imaging, laboratory protection, and compact shielding components. Glasses in the $BaO-Al_2O_3-B_2O_3-WO_3$ system were synthesized by melt quenching with stepwise substitution of B_2O_3 by up to 15 mol.% WO_3, enabling a controlled test of how tungsten modifies a borate-rich network and its functional performance. X-ray diffraction shows a persistent amorphous halo with no detectable devitrification, while FTIR spectra reveal strengthening W–O vibrational features consistent with incorporation of tungsten–oxygen polyhedra, accompanied by depolymerization of the borate network. These structural changes correlate with measurable thermophysical responses, including a rise in linear thermal expansion from 6.65 to 7.54 ppm/^{0}C and a decrease in characteristic temperatures upon incorporation of WO_3. Density increases nearly linearly from 2.868 to 3.578 g/cm^3, whereas molar volume changes weakly, and oxygen packing density decreases from 82.11 to 80.66 mol/L. Photon attenuation improves strongly, with μ increasing by up to 74% (0.399 to 0.694 cm^{-1}) at 0.284 MeV and HVL reduced by about 43% (1.74 to 1.00 cm) at the same energy. The study demonstrates that incremental WO_3 substitution is a practical lead-free route to substantially higher gamma attenuation in barium-aluminum-borate glasses while preserving a stable amorphous state and a workable thermal stability window.

Keywords: borate glasses; lead-free shielding; thermophysical properties; gamma attenuation; melt quenching.

DOI: 10.32434/0321-4095-2026-165-2-91-101

Introduction

The expanding use of ionizing radiation in medical imaging, radiotherapy support infrastructure, industrial radiography, and nuclear research facilities continues to drive the need for effective gamma-ray shielding materials, particularly in applications requiring direct visual access, such as shielded windows, hot cells, and gloveboxes. Transparent shielding materials must combine high photon attenuation efficiency with optical clarity, mechanical reliability, and practical manufacturability. Historically, leaded glasses met this need, but lead's toxicity and end-of-life burdens motivate a shift toward transparent, lead-free alternatives that still deliver high photon attenuation and practical thicknesses along with manufacturability and optical clarity [1]. Glass remains a compelling option for transparent shielding because it is readily melt-processable into large-area panes or complex shapes, can be compositionally tuned across wide property windows, and inherently enables see-through shielding in ways that polymers and many ceramics struggle to deliver at comparable attenuation

levels.

Among lead-free candidates, barium-aluminum-borate glasses offer a practical balance between glass-forming ability and functional performance. Borate networks provide low melting temperatures and high optical transparency, but can suffer from hygroscopicity and limited chemical durability [2]. The incorporation of modifiers and intermediates is a standard route to stabilize the network. In this context, BaO primarily behaves as a network modifier that increases mass density and polarizability while promoting non-bridging oxygens and borate speciation changes, which is beneficial for gamma attenuation [3]. Al_2O_3 often acts as an intermediate/former (AlO_4/AlO_6 units), strengthening connectivity, improving durability, and widening useful thermo-mechanical windows needed for casting and service reliability [4]. As a result, barium-aluminum-borate glasses are being explored not only for shielding-relevant transparency and density but also for broader thermo-optical and sealing/functional glass use-cases where controlled stability against devitrification is essential.

Enhancing the photon shielding performance of borate glasses commonly involves incorporating heavy metal oxide additives with high atomic numbers, such as bismuth, tellurium, and tungsten oxides, which increase both the density and electron concentration of the otherwise light-element borate network, thereby improving photon attenuation efficiency. Tungsten oxide (WO_3) is particularly attractive due to tungsten's high atomic number and ability to integrate into glass networks, increasing density, refractive index, and radiation shielding performance in a range of borate and related glass systems [5]. Moreover, tungsten-containing glasses exhibit favorable thermal, optical, and mechanical properties, enabling applications not only in radiation shielding but also in photonic devices, optical filters, and advanced protective materials [6]. The incorporation of heavy metal oxides such as WO_3 thus represents a key strategy for engineering multifunctional lead-free shielding glasses with enhanced performance and broader applicability.

In this context, the present study comprehensively investigates the substitution of B_2O_3 by WO_3 (up to 15 mol.%) within a $21BaO–9Al_2O_3–(70–n)B_2O_3–nWO_3$ glass system to elucidate how tungsten incorporation modifies the borate network structure and to quantify the resulting changes in thermal properties, density, and gamma-ray shielding performance. The overarching goal is to demonstrate a controllable, lead-free compositional pathway to higher attenuation in barium aluminoborate glasses while maintaining an amorphous state and a workable thermal processing window.

Materials and methods

Glasses in the $BaO–Al_2O_3–B_2O_3–WO_3$ system were prepared by the melt-quench method using the molar composition $21BaO–9Al_2O_3–(70–n)B_2O_3–nWO_3$, where n=0, 2.5, 5, 7.5, 10, 12.5, and 15 mol.% represents stepwise replacement of B_2O_3 by WO_3. Reagent-grade $BaCO_3$ (99%), γ-Al_2O_3 (99.7%), H_3BO_3 (99.6%), and WO_3 (99.99%) were weighed to match each batch, mixed to uniformity, and melted in platinum crucibles at 1350^{0}C for 30 min in a SiC rod-heated furnace. The melts were cast into preheated molds to obtain rods (5×5×50 mm^3) and discs (3 cm diameter), then annealed at 540^{0}C for 5 h and cooled to room temperature at 40^{0}C/h. The glasses were identified according to WO_3 content as BaAlBW0 ($21BaO–9Al_2O_3–70B_2O_3$), BaAlBW2.5 ($21BaO–9Al_2O_3–67.5B_2O_3–2.5WO_3$), BaAlBW5 ($21BaO–9Al_2O_3–65B_2O_3–5WO_3$), BaAlBW7.5 ($21BaO–9Al_2O_3–62.5B_2O_3–7.5WO_3$), BaAlBW10 ($21BaO–9Al_2O_3–60B_2O_3–10WO_3$), BaAlBW12.5 ($21BaO–9Al_2O_3–57.5B_2O_3–12.5WO_3$), and BaAlBW15 ($21BaO–9Al_2O_3–55B_2O_3–15WO_3$).

Thermal characterization was performed by simultaneous thermogravimetric analysis (STA300 Nexta, Hitachi) at 10^{0}C/min to determine the glass transition (T_g) and crystallization peak (T_c) temperatures from DTA curves, and by push-rod dilatometry (GT-1000) at 3^{0}C/min to determine the dilatometric T_g, softening point (T_d), and linear coefficient of thermal expansion (CTE).

Structural features were characterized by XRD (DRON-3M with Co-Kα radiation) and FTIR spectroscopy (Shimadzu IRSpirit-XT, QATR-S accessory, 1800–400 cm^{-1}, 4 cm^{-1} resolution, 30 scans per measurement). Density was measured by Archimedes' technique in decane (ρ=0.732 g/cm^3) using an Axis ANG100 microbalance, and molar volume (V_m) and oxygen packing density (OPD) were calculated from density and batch stoichiometry [3].

Photon shielding performance was then assessed by calculation with the Phy-X software package [7], using the glass compositions and densities as inputs to obtain the μ (linear attenuation coefficient), HVL (half-value layer), MFP (mean free path), and Z_{eff} (effective atomic number) across 0.284–1.333 MeV, covering common gamma energies associated with Cs-137 and Co-60 sources, to track how increasing WO_3 influences attenuation behavior relevant to imaging, laboratory radiation work, and protective materials.

Results and discussion

The amorphous nature of the $BaO–Al_2O_3–$

B_2O_3–WO_3 glasses was examined by X-ray diffraction (Fig. 1). All compositions (BaAlBW0–BaAlBW15) exhibit a broad diffuse halo centered at approximately 30–40⁰ and no sharp Bragg reflections over the measured 2-theta range, indicating the absence of long-range crystalline order. Within the measurement's sensitivity, partial replacement of B_2O_3 with WO up to 15 mol.% did not lead to detectable devitrification under the present melt-quench and annealing conditions. Small differences in the halo profile may suggest changes in the average short-range order, although XRD alone does not allow a detailed description of local structural units. The cast specimens were also visually inspected after annealing. All samples appeared homogeneous without visible inclusions. The color changes from nearly colorless for BaAlBW0 to amber with increasing WO_3 content, which may be related to tungsten-associated optical absorption and possible changes in tungsten coordination or redox state [8].

The structural changes associated with WO_3 incorporation were investigated using ATR-FTIR spectroscopy (Fig. 2). The spectra display the broad, overlapping bands characteristic of multi-component borate-based glasses. Band assignments in such systems are not unique because several vibrational modes can contribute within the same wavenumber region. Therefore, the discussion below focuses on commonly accepted spectral regions and compositional trends rather than on one-to-one identification of specific borate superstructural units. In the high-wavenumber region (1200–1400 cm^{-1}), the prominent bands centered at approximately 1342 cm^{-1} and 1208 cm^{-1} correspond to the asymmetric B–O stretching vibrations of trigonal BO_3 units [9], specifically those associated with metaborate and pyroborate species containing non-bridging oxygens (NBOs). The intermediate-frequency region (800–1100 cm^{-1}) provides critical information on tetrahedral borate units and tungstate incorporation. The bands at 1094 cm^{-1} and 1018 cm^{-1} are assigned to the B–O stretching vibrations of four-coordinated BO_4 tetrahedra, which form stable diborate and pentaborate groupings within the network [10]. As WO_3 incorporation increases, the relative intensity of the 1018 cm^{-1} band diminishes, suggesting a gradual conversion of BO_4 tetrahedra back toward trigonal BO_3 coordination. A similar trend is commonly observed in modified borate systems and indicates network depolymerization [11]. Additional spectral features appear and become more pronounced in the 922 to 860 cm^{-1} region as WO_3 increases. In tungsten-containing glasses, absorptions in this interval are often assigned to W–O related stretching vibrations from tungstate-like structural units, which are frequently described as distorted WO_x polyhedra [12]. The gradual shift of these features

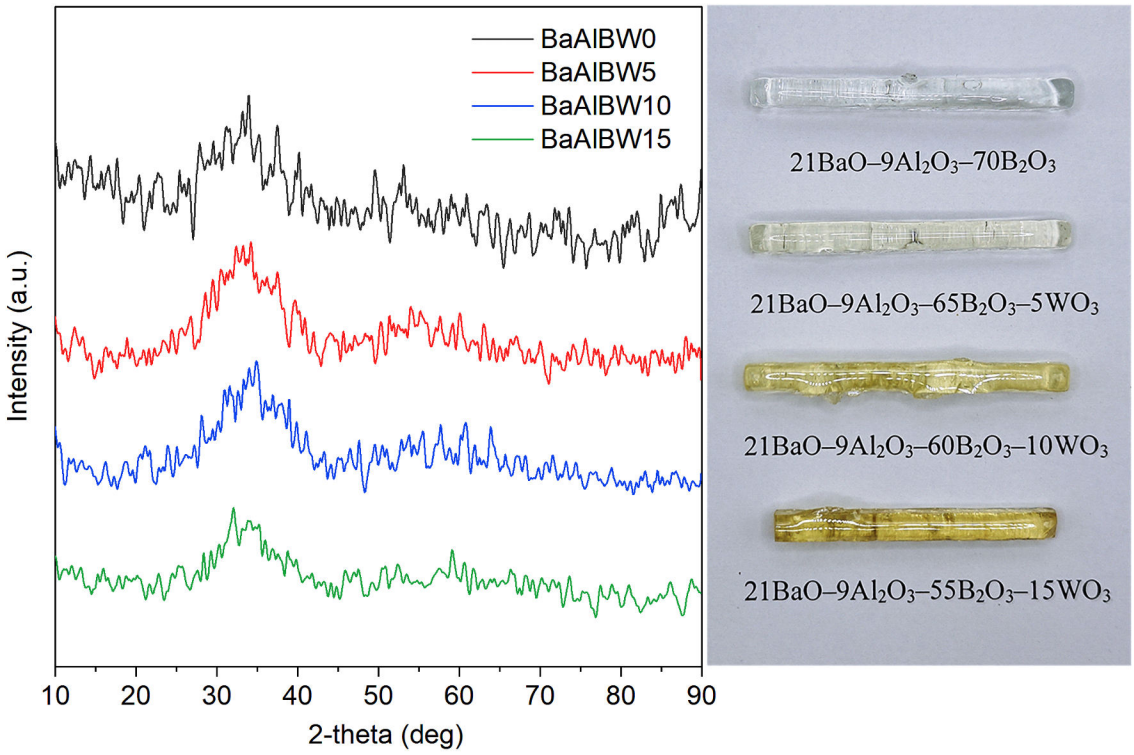

Fig. 1. Effect of WO_3-for-B_2O_3 substitution on XRD signatures and physical appearance of BaAlBW glasses

toward lower wavenumbers with composition may reflect changes in the tungsten oxygen coordination environment and an increase in the fraction of tungsten-related units within the glass structure. At the same time, the reduction of BO_4-related intensity indicates that substitution of B_2O_3 by WO_3 drives a coupled rearrangement of the borate and tungstate substructures. The band observed at approximately 686 cm^{-1} is attributable to B–O–B bending vibrations involving bridging oxygen atoms within various borate segments, while the feature near 463 cm^{-1} likely comprises overlapping contributions from O–B–O bending modes and Ba–O stretching vibrations associated with the network modifier cations [13]. Collectively, these spectroscopic signatures indicate that substituting B_2O_3 with WO_3 induces a complex structural reorganization involving the conversion of tetrahedral borate units to trigonal configurations, the incorporation of tungstate polyhedra into the structure, and an overall loosening of the network structure through increased non-bridging oxygen content.

The physical manifestation of this structural reorganization is reflected in the density and molar volume trends shown in Fig. 3. The measured density increases nearly linearly from 2.868 g/cm^3 (BaAlBW0) to 3.578 g/cm^3 (BaAlBW15), indicative of an approximate 25% augmentation over the investigated range, which is consistent with the introduction of a heavier oxide component and an increase in the average formula mass. In contrast, the molar volume changes only modestly, increasing from 31.42 to 31.99 cm^3/mol and approaching a plateau above 12.5 mol.% WO_3. The concurrent increase in density and V_m implies that the mass gain associated with WO_3 incorporation outweighs a small expansion of the molar volume, which is compatible with incorporation of WO_x polyhedra and the network rearrangement inferred from FTIR. The oxygen packing density, defined here as the number of oxygen moles per unit volume, decreases from 82.11 to 80.66 mol/L as WO_3 increases. In the context of the FTIR trends (reduced BO_4 contribution and the emergence of W–O bands), the concurrent increase in V_m and decrease in OPD is consistent with a gradual opening of the borate network as tungstate-related structural units are incorporated, even as the overall density increases due to tungsten's high atomic mass.

In line with the molar volume increase and OPD decrease, dilatometry indicates lower characteristic temperatures and a higher CTE with increasing WO_3. Dilatometric trace for the base BaAlBW0 composition (Fig. 4) displays the characteristic expansion profile typical of borate-rich glasses, transitioning from rigid glassy behavior to pronounced viscous deformation as the temperature approaches the softening point. Across the compositional series, substituting B_2O_3 with WO_3

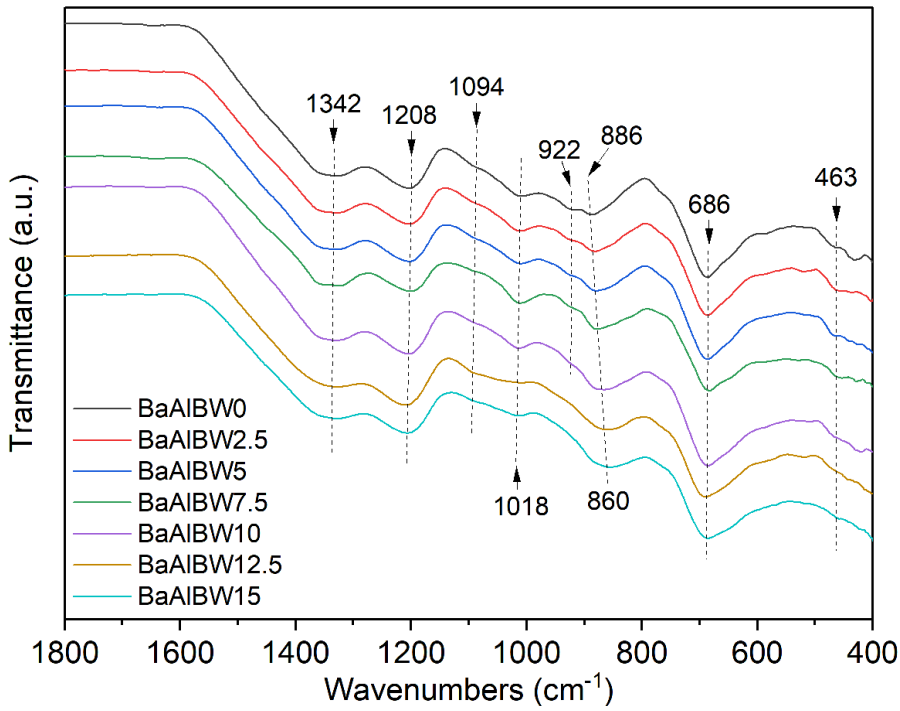

Fig. 2. ATR-FTIR spectra of BaO–Al_2O_3–B_2O_3–WO_3 glasses showing structural evolution with WO_3 content

produces a monotonic increase in $CTE_{20–400}$ from 6.65 to 7.54 ppm/^{0}C (0–15 mol.% WO_3), while both dilatometric T_g and T_d decrease from 539 to 515^{0}C and from 576 to 542^{0}C, respectively. The concurrent rise in CTE and depression of T_g/T_d is consistent with a modest reduction in network rigidity, in line with the FTIR-indicated shift toward more BO_3/NBO-bearing environments and the OPD

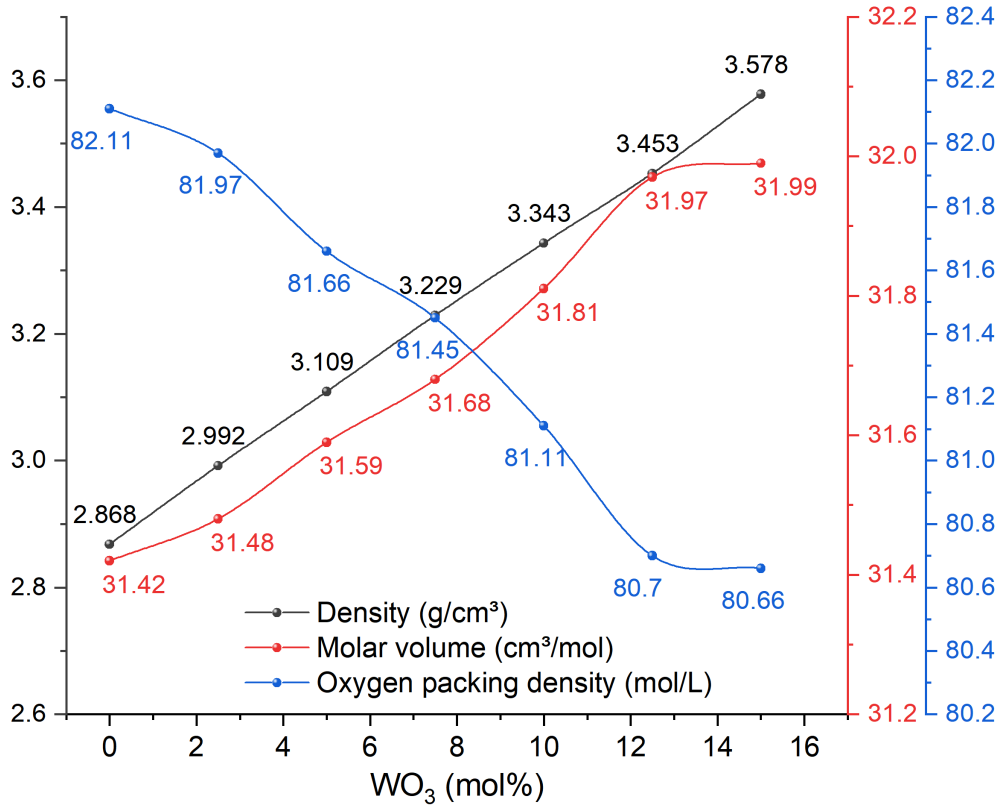

Fig. 3. Physical property trends versus WO_3 concentration for the BaAlBW series

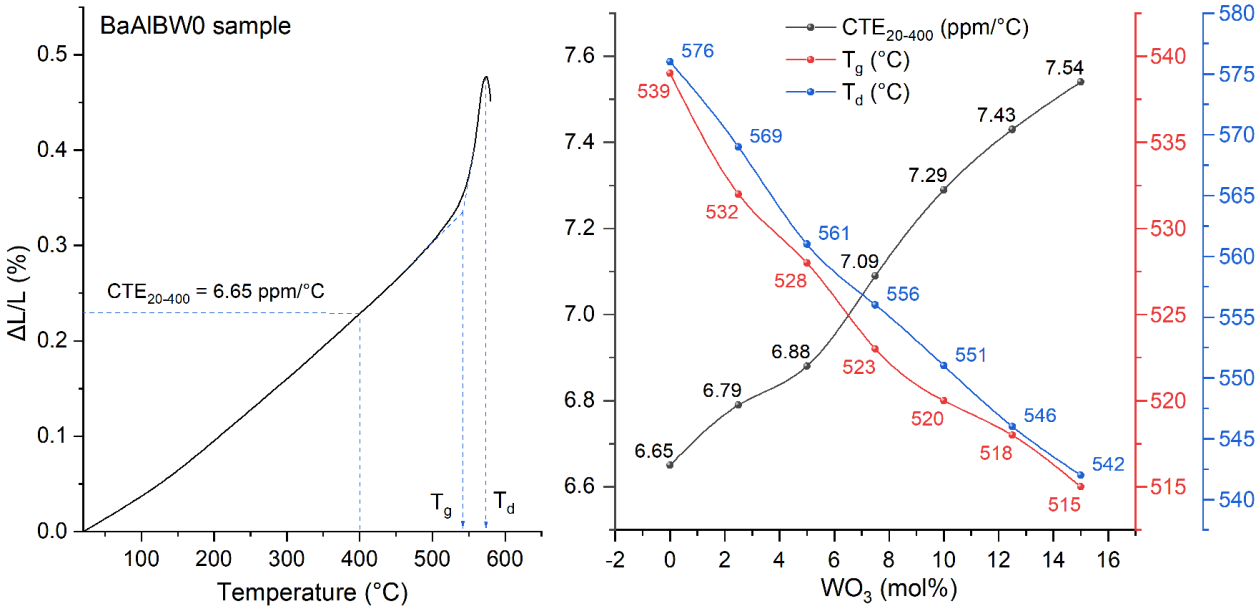

Fig. 4. Dilatometry of BaAlBW glasses: expansion curve (BaAlBW0) and WO_3-dependent thermal parameters

decrease. The temperature interval between T_d and T_g also contracts from ~37°C (WO_3=0–2.5 mol.%) to ~27°C (WO_3=15 mol.%), suggesting a narrower viscoelastic working window at higher WO_3 contents under the present measurement conditions.

To complement the dilatometric evidence for a narrowing working interval at higher WO_3 contents, the DTA thermograms in Fig. 5 track how the glass transition and crystallization events shift with composition. Each sample shows a clear endothermic baseline change assigned to the glass transition temperature (T_g) followed at higher temperature by an exothermic crystallization peak (T_c). Across the BaAlBW series, T_g decreases gradually from 536°C (BaAlBW0) to 518°C (BaAlBW15), consistent with the reduced network rigidity inferred from FTIR and the T_g depression measured by dilatometry. A comparable trend is observed for crystallization, with T_c shifting from 673°C (BaAlBW0) to 625°C (BaAlBW15). Consistent with this shift, the separation $\Delta T = T_c - T_g$ contracts overall from 137°C (BaAlBW0) to 107°C (BaAlBW15), which suggests that modest WO_3 additions do not immediately reduce stability but higher WO_3 contents narrow the supercooled-liquid interval before crystallization. Taken together, Figure 5 supports the view that substituting B_2O_3 with WO_3 lowers the characteristic relaxation temperature and shifts the dominant crystallization event to lower temperatures, aligning with the broader picture of a more weakly constrained, NBO-richer network at higher tungsten content.

Building on the density increase observed with WO_3 substitution, the photon shielding response was quantified using the calculated linear attenuation coefficient, μ (cm^{-1}), as a function of energy (Fig. 6). For all compositions, μ decreases with energy, with the steepest decline at low energies (0.284–0.347 MeV) and a more gradual decrease toward 2.506 MeV, consistent with a reduced contribution of photoelectric absorption as the interaction regime shifts toward Compton scattering [14]. Superimposed on this energy dependence is a clear compositional ordering: at every energy, higher WO_3 content yields higher μ, and the separation between curves is most pronounced at low energies. At 0.284 MeV, μ rises from 0.399 cm^{-1} for BaAlBW0 to 0.694 cm^{-1} for BaAlBW15, corresponding to an increase of about 0.295 cm^{-1}, or roughly 74% relative to the base glass. The same trend persists at 0.347 MeV, where μ increases from 0.333 to 0.529 cm^{-1}, and remains clearly resolved at 0.662 MeV, a representative energy for Cs-137, where μ increases from 0.219 to 0.292 cm^{-1}, about a 33% gain. In the Co-60 energy region, the improvement persists with a smaller relative gain: μ increases from 0.160 to 0.202 cm^{-1} at 1.173 MeV (about 26%), and from 0.150 to

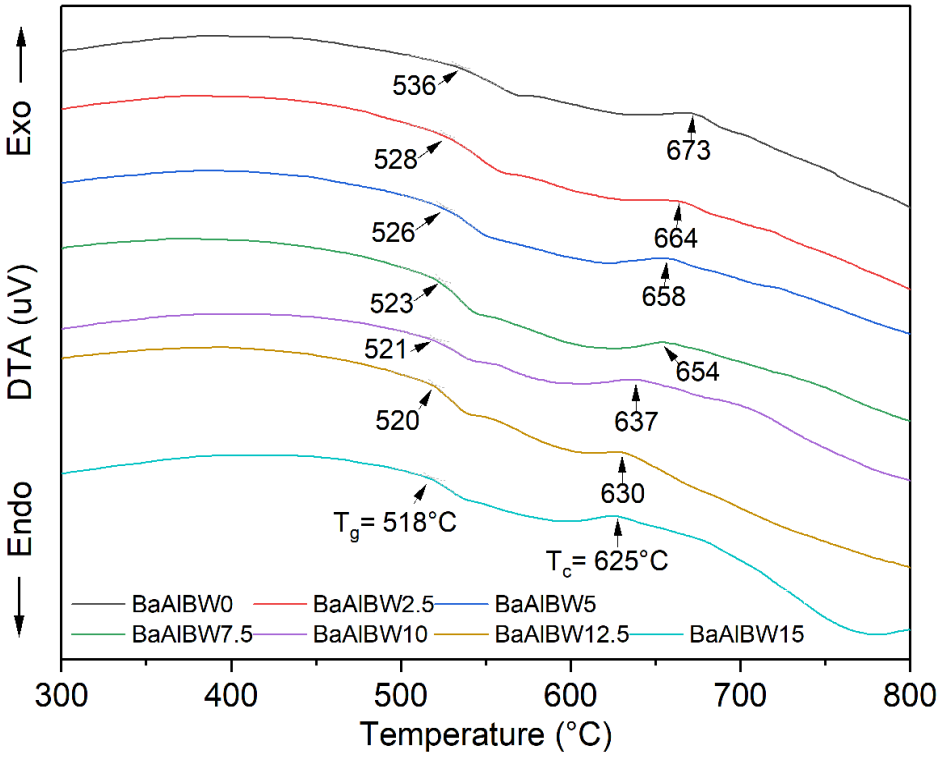

Fig. 5. DTA thermograms of BaAlBW glasses

0.188 cm^{-1} at 1.333 MeV (about 25%). Even at the highest energy reported (2.506 MeV), μ rises from 0.110 to 0.141 cm^{-1} (about 28%). Overall, the data indicate that replacing B_2O_3 with WO_3 provides a robust, composition-controlled enhancement in γ-ray attenuation, driven by the combined effects of increased density and the higher atomic-number contribution of tungsten, with the strongest relative gains occurring at lower energies, where photoelectric interactions are more sensitive to composition.

Figure 7 extends the attenuation analysis by recasting m into the more application-oriented thickness metrics, the half-value layer (HVL, the thickness required to reduce the incident photon intensity by 50%) and the mean free path (MFP, the average distance between successive photon interactions) [15] of the $BaO-Al_2O_3-B_2O_3-WO_3$ glasses as functions of photon energy. Figures 7a and 7b show that both HVL and MFP increase with photon energy for every composition, reflecting the reduced interaction probability as the dominant mechanism shifts away from photoelectric absorption and toward Compton scattering in this energy range. Superimposed on this energy dependence is a clear compositional ranking: at each energy, higher WO_3 content yields lower HVL and lower MFP, mirroring the ordering observed in μ. At the lowest energy (0.284 MeV), the separation between compositions is largest. HVL decreases from 1.74 cm for BaAlBW0 to 1.00 cm for BaAlBW15, a reduction of 0.74 cm (approximately 43% reduction), while MFP drops from 2.51 to 1.44 cm, aligning with the inset bar charts. This is a practically meaningful change: for the same attenuation target, the WO_3-rich glasses would require substantially less thickness than the tungsten-free baseline, consistent with the strong dependence of low-energy attenuation on atomic number (Z) and density. The same pattern persists at 0.347 MeV, where HVL decreases from 2.08 to 1.31 cm and MFP from 3.01 to 1.89 cm. By 0.662 MeV, the absolute values increase, but WO_3 substitution still provides a distinct reduction: HVL decreases from 3.17 cm (BaAlBW0) to 2.37 cm

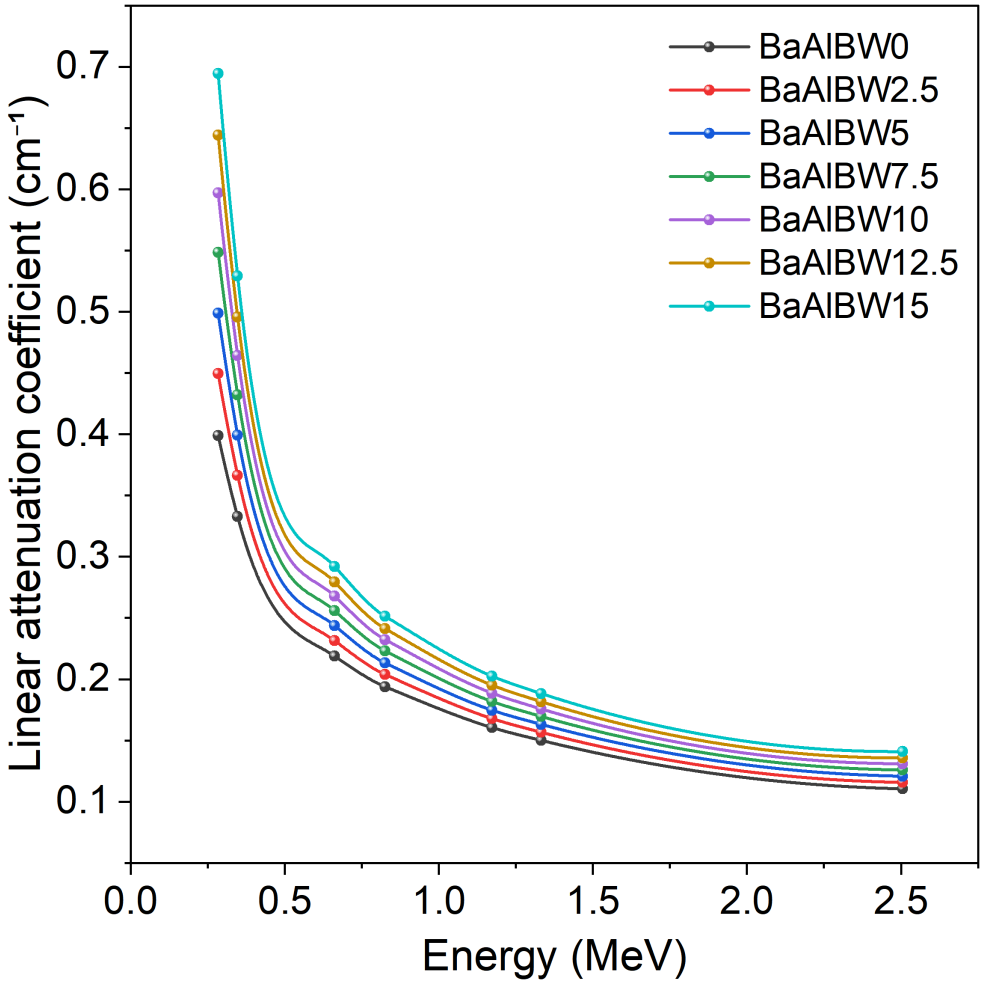

Fig. 6. Energy and composition dependence of linear attenuation coefficient in $BaO-Al_2O_3-B_2O_3-WO_3$ glasses

(BaAlBW15), and MFP decreases from 4.57 to 3.43 cm (approximately 25%). Thus, the compositional benefit remains evident in the intermediate-energy region where Compton scattering dominates, although the relative gain is smaller than at 0.284–0.347 MeV. Even at the highest energy reported (2.506 MeV), where Compton scattering dominates and composition effects are expected to be muted, the ordering is preserved: HVL is reduced from 6.28 to 4.92 cm and MFP from 9.05 to 7.10 cm when moving from BaAlBW0 to BaAlBW15. Taken together, the HVL and MFP results support the interpretation that WO_3 addition yields a consistent, composition-controlled reduction in the shielding thickness needed across the investigated energies, with the strongest practical gains appearing at the lower-energy end where the composition sensitivity of γ-interactions is greatest.

Figure 8 provides a complementary analysis to the HVL and MFP trends by demonstrating how the effective atomic number (a single-number indicator of how strongly each glass interacts with gamma rays) varies with photon energy for the $BaO–Al_2O_3–B_2O_3–WO_3$ glasses. Across all compositions, Z_{eff} is highest at the lowest investigated energy and then decreases rapidly between 0.284 and 0.662 MeV before approaching a broad minimum near the Co-60 energy range (approx. 1.17–1.33 MeV) and exhibiting a modest upturn at 2.506 MeV. For the tungsten-free glass (BaAlBW0), Z_{eff} drops from 12.35 at 0.284 MeV to 10.06 at 0.662 MeV and reaches its lowest values near 1.173–1.333 MeV (9.76–9.74), followed by a modest increase to 9.98 at 2.506 MeV. The modest rise at 2.506 MeV plausibly reflects the onset of pair production above 1.022 MeV, which reintroduces a stronger dependence on Z as energy increases, even though pair production is not yet dominant at a few MeV. Superimposed on this energy dependence is a clear compositional effect: at every energy, increasing WO_3 shifts Z_{eff} upward, reflecting tungsten's high atomic number and its growing weight fraction in the glass network. Quantitatively, at 0.284 MeV, Zeff rises from 12.35 (BaAlBW0) to 20.47 (BaAlBW15), while at 0.347 MeV, it increases from 11.37 to 17.80. These large separations align with the stronger low-energy sensitivity to high-Z constituents. In the Co-60 range, Z_{eff} values cluster more tightly while preserving the same ordering (e.g., 9.76 to 12.87 at 1.173 MeV and 9.74 to 12.80 at 1.333 MeV), consistent with reduced but persistent composition leverage at higher energies. The slight increase at 2.506 MeV (9.98 to 13.26) suggests that tungsten-rich glasses retain an advantage as energy moves further into the pair-production-accessible regime. Overall, Figure 8 reinforces the attenuation and thickness metrics by showing that WO_3 substitution increases the interaction-relevant atomic number across the full energy window, with the largest gains concentrated at lower energies where shielding thickness is most sensitive to composition.

Conclusions

A series of seven $21BaO–9Al_2O_3–(70–n)B_2O_3–nWO_3$ glasses ($0 \le n \le 15$ mol.%) was produced by melt–quench processing and remained XRD-amorphous across the full substitution range, indicating that WO_3 incorporation up to 15 mol.% does not trigger

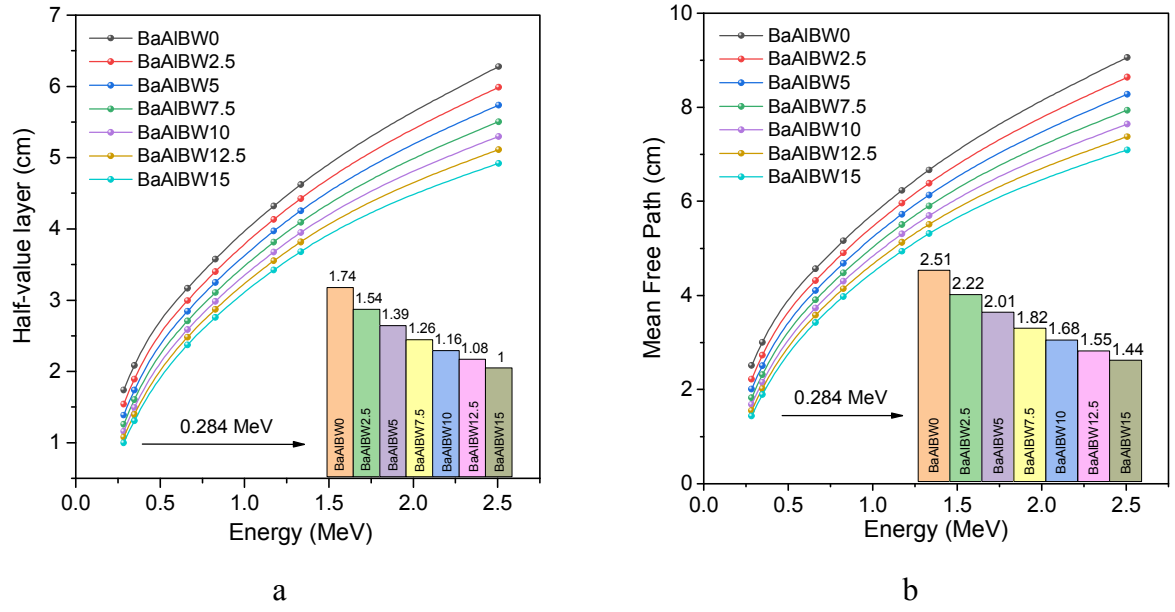

Fig. 7. Energy and composition dependence of HVL (a) and MFP (b) in $BaO–Al_2O_3–B_2O_3–WO_3$ glasses

detectable devitrification under the reported melting, casting, and annealing schedule. FTIR spectra show attenuation of BO_4-associated contributions alongside the growth of W–O vibrational features, indicating incorporation of WO_x polyhedra and accompanying reorganization of the borate network toward lower connectivity. Structurally driven property changes are coherent: density increases from 2.868 to 3.578 g/cm^3, while V_m rises only slightly (31.42 to 31.99 cm^3/mol) and OPD decreases (82.11 to 80.66 mol/L), implying heavier compositions with modest network opening. From an applications standpoint, the principal benefit is thickness reduction at medically and industrially relevant energies. At 0.662 MeV (Cs-137), HVL decreased from 3.17 to 2.37 cm and μ increased from 0.219 to 0.292 cm^{-1}. In the Co-60 window, μ rose from 0.150 to 0.188 cm^{-1} at 1.333 MeV, and the advantage persisted to 2.506 MeV, where HVL fell from 6.28 to 4.92 cm. Effective atomic number increased concurrently (e.g., 9.74 to 12.80 at 1.333 MeV), supporting the sustained high-Z contribution of tungsten even where Compton scattering dominates. These shielding gains are coupled to a narrower thermal processing window: CTE increased from 6.65 to 7.54 ppm/^{0}C, dilatometric T_g decreased from 539 to 515^{0}C and T_d from 576 to 542^{0}C, while the stability interval ΔT contracted from 137 to 107^{0}C, suggesting reduced resistance to crystallization during heating in the WO_3-rich compositions (12.5–15 mol.% WO_3). Overall, WO_3 provides an effective lever to engineer borate glasses for compact shielding with manageable thermal penalties.

REFERENCES

1. *AbuAlRoos N.J., Baharul Amin N.A., Zainon R.* Conventional and new lead-free radiation shielding materials for radiation protection in nuclear medicine: a review // Radiat. Phys. Chem. – 2019. – Vol.165. – Art. No. 108439.

2. *Carneiro G.N., Vargas H., Sampaio J.A.* Thermo-optical and structural properties of barium aluminoborate glasses // J. Alloys Compd. – 2019. – Vol.777. – P.1327-1333.

3. *Hordieiev Y., Zaichuk A.* Impact of La_2O_3 substitution on the structural, thermal, and radiation shielding properties of sodium–barium borosilicate glasses // Int. J. Ceram. Eng. Sci. – 2025. – Vol.7. – Art. No. e70029.

4. *Hordieiev Y.S., Zaichuk A.V.* Effect of the addition of Al_2O_3, ZnO and TiO_2 on the crystallization behavior, thermal and some physical properties of lead borate glasses // MRS Adv. – 2023. – Vol.8. – P.201-206.

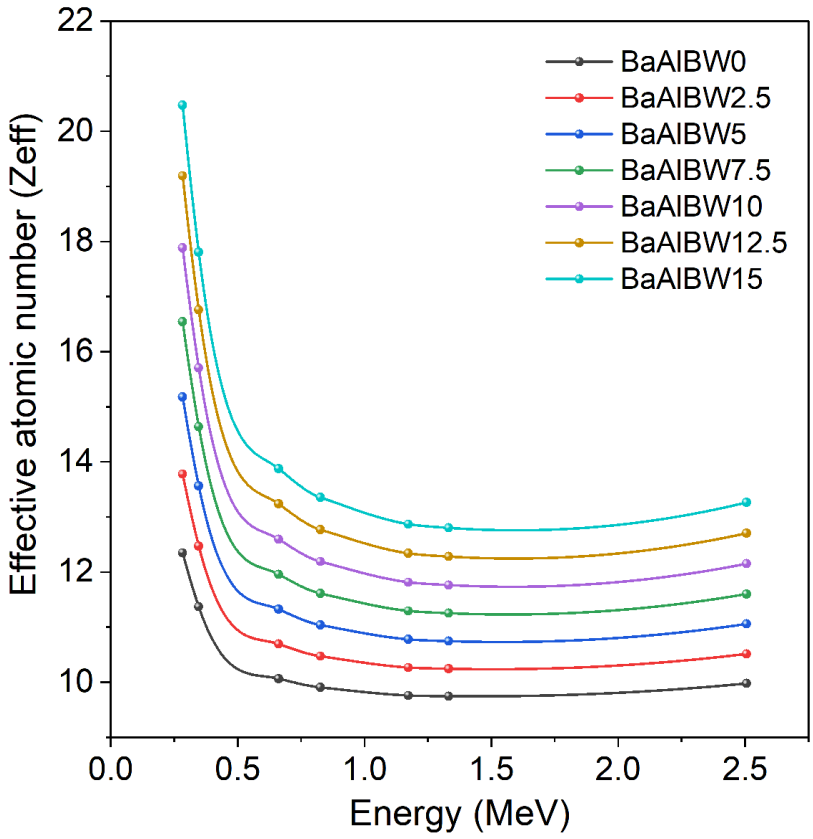

Fig. 8. Energy and composition dependence of Z_{eff} in $BaO–Al_2O_3–B_2O_3–WO_3$ glasses

5. *Optical* and structural characterization of WO_3 modified B_2O_3-based glassy composites for radiation shielding applications / Elqahtani Z.M., Iliyasu U., Shehu A., El-Rayyes A., Al-Buriahi M.S. // Ceram Int. – 2025. – Vol.51. – P.29655-29667.

6. *Tungsten-doped* borosilicate glasses for radiation shielding / Suriyoporn S., Suwanprateep S., Sawangboon N., Chuamsaamarkkee K., Charoenphun P., Meechoowas E. // Curr. Appl. Sci. Technol. – 2024. – Vol.25. – Art. No. e0262195.

7. *Phy-X/PSD*: development of a user friendly online software for calculation of parameters relevant to radiation shielding and dosimetry / Sakar E., Ozpolat O.F., Alim B., Sayyed M.I., Kurudirek M. // Radiat. Phys. Chem. – 2020. – Vol.166. – Art. No. 108496.

8. *Reversible* 3D optical data storage and information encryption in photo-modulated transparent glass medium / Hu Z., Huang X., Yang Z., Qiu J., Song Z., Zhang J., Dong G. // Light Sci. Appl. – 2021. – Vol.10. – Art. No. 140.

9. *Hordieiev Y.S., Zaichuk A.V.* Enhanced gamma-ray shielding and thermal-physical properties in novel zinc yttrium borate glasses // Dig. J. Nanomater. Biostruct. – 2025. – Vol.20. – P.901-911.

10. *Hordieiev Y., Zaichuk A.* Structural, thermal, and radiation shielding properties of antimony-doped zinc borate glasses // Sci. Rep. – 2025. – Vol.15. – Art. No. 16158.

11. *Kamitsos E.I., Chryssikos G.D.* Borate glass structure by Raman and infrared spectroscopies // J. Mol. Struct. – 1991. – Vol.247. – P.1-16.

12. *Raman*, FTIR studies and optical absorption of zinc borate glasses containing WO_3 / Farouk M., Samir A., Ibrahim A., Farag M.A., Solieman A. // Appl. Phys. A Mater. Sci. Process. – 2020. – Vol.126. – Art. No. 696.

13. *Properties* and structural characteristics of glasses in the $SrO–BaO–Al_2O_3–B_2O_3–SiO_2$ system for dielectric composite materials / Amelina O.A., Zaichuk O.V., Hordieiev Y.S., Filonenko D.V., Kalishenko Y.R. // Voprosy Khimii i Khimicheskoi Tekhnologii. – 2024. – No. 6. – P.47-54.

14. *Gamma* attenuation, buildup factors, and radiation shielding performance of CaO-borosilicate glasses / Alrowaili Z.A., Echeweozo E.O., Alomairy S., Hammoud A., Sriwunkum C., Alsaiari N.S., Boukhris I., Al-Buriahi M.S. // J. Radiat. Res. Appl. Sci. – 2025. – Vol.18. – Art. No. 101221.

15. *Sayyed M.I., Olarinoye O.I., Elsafi M.* Assessment of gamma-radiation attenuation characteristics of $Bi_2O_3–B_2O_3–SiO_2–Na_2O$ glasses using Geant4 simulation code // Eur. Phys. J. Plus. – 2021. – Vol.136. – Art. No. 535.

Received 30.12.2025
Revised 20.03.2026
Accepted 30.03.2026
Published 28.04.2026

ВОЛЬФРАМ-МОДИФІКОВАНІ БАРІЙ-АЛЮМІНІЙ-БОРАТНІ СТЕКЛА З РЕГУЛЬОВАНОЮ ТЕПЛОВОЮ ПОВЕДІНКОЮ ТА ПІДВИЩЕНИМ ЕКРАНУВАННЯМ ГАММА-ВИПРОМІНЮВАННЯ

Ю.С. Гордєєв, О.В. Зайчук

Радіаційно-захисне скло, що не містить свинцю, але забезпечує високу ефективність ослаблення гамма-випромінювання, залишається пріоритетним матеріалом для медичної візуалізації, лабораторного захисту та створення компактних екрануючих компонентів. Скло системи $BaO–Al_2O_3–B_2O_3–WO_3$ синтезовано методом гартування з розплаву із поступовим заміщенням B_2O_3 на WO_3 (до 15 мол.%), що дозволило дослідити вплив вольфраму на структуру боратної скляної мережі та функціональні властивості скла. Дані рентгенівської дифракції підтверджують збереження аморфного стану, про що свідчить наявність характерного аморфного гало без ознак девітрифікації. Інфрачервоні спектри демонструють посилення коливальних смуг зв'язків W–O, що узгоджується з формуванням вольфрамо-кисневих координаційних поліедрів і супроводжується деполімеризацією боратної сітки. Встановлено, що ці структурні зміни корелюють із вимірюваними термофізичними властивостями, зокрема зі збільшенням коефіцієнта лінійного теплового розширення від 6,65 до 7,54 ppm/^{0}C та зниженням характеристичних температур зі збільшенням вмісту WO_3. Густина скла зростає майже лінійно від 2,868 до 3,578 г/см^3, тоді як молярний об'єм змінюється незначно, а щільність упаковки кисню зменшується від 82,11 до 80,66 моль/л. Ефективність ослаблення фотонного випромінювання істотно підвищується: лінійний коефіцієнт ослаблення μ зростає до 74% (від 0,399 до 0,694 см$^{-1}$) при енергії 0,284 МеВ, тоді як товщина половинного ослаблення зменшується приблизно на 43% (від 1,74 до 1,00 см) за тієї ж енергії. Отримані результати демонструють, що введення WO_3 є ефективною безсвинцевою стратегією істотного підвищення ефективності екранування гамма-випромінювання в барій–алюміній–боратних стеклах при збереженні стабільного аморфного стану та достатнього інтервалу термічної стабільності.

Ключові слова: боратне скло, безсвинцеве екранування, теплофізичні властивості, ослаблення гамма-випромінювання, гартування з розплаву.

TUNGSTEN-MODIFIED BARIUM-ALUMINUM-BORATE GLASSES WITH TUNABLE THERMAL BEHAVIOR AND ENHANCED GAMMA-RAY SHIELDING

Yu.S. Hordieiev* *, *A.V. Zaichuk

Ukrainian State University of Science and Technologies, Dnipro, Ukraine

* **e-mail: yuriihordieiev@gmail.com**

Radiation shielding glasses that avoid lead while retaining high attenuation efficiency remain a materials priority for medical imaging, laboratory protection, and compact shielding components. Glasses in the $BaO-Al_2O_3-B_2O_3-WO_3$ system were synthesized by melt quenching with stepwise substitution of B_2O_3 by up to 15 mol.% WO_3, enabling a controlled test of how tungsten modifies a borate-rich network and its functional performance. X-ray diffraction shows a persistent amorphous halo with no detectable devitrification, while FTIR spectra reveal strengthening W–O vibrational features consistent with incorporation of tungsten–oxygen polyhedra, accompanied by depolymerization of the borate network. These structural changes correlate with measurable thermophysical responses, including a rise in linear thermal expansion from 6.65 to 7.54 ppm/^{0}C and a decrease in characteristic temperatures upon incorporation of WO_3. Density increases nearly linearly from 2.868 to 3.578 g/cm^3, whereas molar volume changes weakly, and oxygen packing density decreases from 82.11 to 80.66 mol/L. Photon attenuation improves strongly, with μ increasing by up to 74% (0.399 to 0.694 cm^{-1}) at 0.284 MeV and HVL reduced by about 43% (1.74 to 1.00 cm) at the same energy. The study demonstrates that incremental WO_3 substitution is a practical lead-free route to substantially higher gamma attenuation in barium-aluminum-borate glasses while preserving a stable amorphous state and a workable thermal stability window.

Keywords: borate glasses; lead-free shielding; thermophysical properties; gamma attenuation; melt quenching.

REFERENCES

1. AbuAlRoos NJ, Baharul Amin NA, Zainon R. Conventional and new lead-free radiation shielding materials for radiation protection in nuclear medicine: a review. *Radiat Phys Chem.* 2019; 165: 108439. doi: 10.1016/j.radphyschem.2019.108439.

2. Carneiro GN, Vargas H, Sampaio JA. Thermo-optical and structural properties of barium aluminoborate glasses. *J Alloys Compd.* 2019; 777: 1327-1333. doi: 10.1016/j.jallcom.2018.11.044.

3. Hordieiev Y, Zaichuk A. Impact of La_2O_3 substitution on the structural, thermal, and radiation shielding properties of sodium–barium borosilicate glasses. *Int J Ceram Eng Sci.* 2025; 7: e70029. doi: 10.1002/ces2.70029.

4. Hordieiev YS, Zaichuk AV. Effect of the addition of Al_2O_3, ZnO and TiO_2 on the crystallization behavior, thermal and some physical properties of lead borate glasses. *MRS Adv.* 2023; 8: 201-206. doi: 10.1557/s43580-023-00511-7.

5. Elqahtani ZM, Iliyasu U, Shehu A, El-Rayyes A, Al-Buriahi MS. Optical and structural characterization of WO_3 modified B_2O_3-based glassy composites for radiation shielding applications. *Ceram Int.* 2025; 51: 29655-29667. doi: 10.1016/j.ceramint.2025.04.168.

6. Suriyoporn S, Suwanprateep S, Sawangboon N, Chuamsaamarkkee K, Charoenphun P, Meechoowas E. Tungsten-doped borosilicate glasses for radiation shielding. *Curr Appl Sci Technol.* 2024; 25: e0262195. doi: 10.55003/cast.2024.262195.

7. Sakar E, Ozpolat OF, Alim B, Sayyed MI, Kurudirek M. Phy-X/PSD: development of a user friendly online software for calculation of parameters relevant to radiation shielding and dosimetry. *Radiat Phys Chem.* 2020; 166: 108496. doi: 10.1016/j.radphyschem.2019.108496.

8. Hu Z, Huang X, Yang Z, Qiu J, Song Z, Zhang J, et al. Reversible 3D optical data storage and information encryption in photo-modulated transparent glass medium. *Light Sci Appl.* 2021; 10: 140. doi: 10.1038/s41377-021-00581-y.

9. Hordieiev YS, Zaichuk AV. Enhanced gamma-ray shielding and thermal-physical properties in novel zinc yttrium borate glasses. *Dig J Nanomater Biostruct.* 2025; 20: 901-911. doi: 10.15251/djnb.2025.203.901.

10. Hordieiev Y, Zaichuk A. Structural, thermal, and radiation shielding properties of antimony-doped zinc borate glasses. *Sci Rep.* 2025; 15: 16158. doi: 10.1038/s41598-025-96015-5.

11. Kamitsos EI, Chryssikos GD. Borate glass structure by Raman and infrared spectroscopies. *J Mol Struct.* 1991; 247: 1-16. doi: 10.1016/0022-2860(91)87058-p.

12. Farouk M, Samir A, Ibrahim A, Farag MA, Solieman A. Raman, FTIR studies and optical absorption of zinc borate glasses containing WO_3. *Appl Phys A Mater Sci Process.* 2020; 126: 696. doi: 10.1007/s00339-020-03890-y.

13. Amelina OA, Zaichuk OV, Hordieiev YS, Filonenko DV, Kalishenko YR. Properties and structural characteristics of glasses in the $SrO-BaO-Al_2O_3-B_2O_3-SiO_2$ system for dielectric composite materials. *Voprosy Khimii i Khimicheskoi Tekhnologii.* 2024; (6): 47-54. doi: 10.32434/0321-4095-2024-157-6-47-54.

14. Alrowaili ZA, Echeweozo EO, Alomairy S, Hammoud A, Sriwunkum C, Alsaiari NS, et al. Gamma attenuation, buildup factors, and radiation shielding performance of CaO-borosilicate glasses. *J Radiat Res Appl Sci.* 2025; 18: 101221. doi: 10.1016/j.jrras.2024.101221.

15. Sayyed MI, Olarinoye OI, Elsafi M. Assessment of gamma-radiation attenuation characteristics of $Bi_2O_3-B_2O_3-SiO_2-Na_2O$ glasses using Geant4 simulation code. *Eur Phys J Plus.* 2021; 136: 535. doi: 10.1140/epjp/s13360-021-01492-y.